Structural Basis for Lipid Binding and Function by an Evolutionarily Conserved Protein, Serum Amyloid A

Nicholas M. Frame[1], Meera Kumanan[2], Thomas E. Wales[3], Asanga Bandara[2], Marcus Fändrich[4], John E. Straub[2], John R. Engen[3] and Olga Gursky[1,5]

1 - Department of Physiology & Biophysics, *Boston University School of Medicine, 700 Albany Street, Boston, MA, 02118, United States*
2 - Department of Chemistry, *Boston University, 590 Commonwealth Avenue, Boston, MA, 02215, United States*
3 - Department of Chemistry and Chemical Biology, *Northeastern University, 360 Huntington Avenue, Boston, MA, 02115, United States*
4 - Institute of Protein Biochemistry, *Ulm University, Ulm, 89081, Germany*
5 - Amyloidosis Treatment and Research Center, *Boston University School of Medicine, Boston, MA, 02118, United States*

Correspondence to Olga Gursky, John R. Engen, and John E. Straub: *Department of Physiology & Biophysics, Boston University School of Medicine, W302, 700 Albany St., Boston, MA, 02118, USA. straub@bu.edu, J.Engen@northeastern.edu, gursky@bu.edu.*
https://doi.org/10.1016/j.jmb.2020.01.029
Edited by Sheena E Radford

Abstract

Serum amyloid A (SAA) is a plasma protein that transports lipids during inflammation. To explore SAA solution conformations and lipid-binding mechanism, we used hydrogen-deuterium exchange mass spectrometry, lipoprotein reconstitution, amino acid sequence analysis, and molecular dynamics simulations. Solution conformations of lipid-bound and lipid-free mSAA1 at pH~7.4 agreed in details with the crystal structures but also showed important differences. The results revealed that amphipathic α-helices h1 and h3 comprise a lipid-binding site that is partially pre-formed in solution, is stabilized upon binding lipids, and shows lipid-induced folding of h3. This site sequesters apolar ligands via a concave hydrophobic surface in SAA oligomers. The largely disordered/dynamic C-terminal region is conjectured to mediate the promiscuous binding of other ligands. The h1-h2 linker region is predicted to form an unexpected β-hairpin that may represent an early amyloidogenic intermediate. The results help establish structural underpinnings for understanding SAA interactions with its key functional ligands, its evolutional conservation, and its transition to amyloid.

Introduction

Serum amyloid A (SAA) is a major acute-phase protein that is a biomarker of inflammation [1,2] and the protein precursor of amyloid A (AA) that causes AA amyloidosis, a life-threatening complication of chronic inflammation [3,4]. Elevated SAA is a causative factor for atherosclerosis [5]. SAA comprises a family of ~12 kDa proteins that have been highly evolutionally conserved for at least 5,000,000 years and is proposed to play an essential role in the inflammatory response [6,7] (Fig. 1). In humans and other mammals, SAA is secreted by the liver into plasma and is also produced by various extrahepatic tissues at the inflammation sites [8,9]. Hours after the onset of infection or injury, plasma levels of inducible SAA increase nearly a thousand-fold, reaching up to 3 mg/ml, and then rapidly decrease [1,7,10,11]. The beneficial role of these spikes in SAA levels is unclear and probably relates to lipid transport.

Most circulating SAA binds to plasma high-density lipoproteins (HDL) and reroutes HDL transport [12,13]. Like other HDL proteins, SAA is water-soluble and is transiently released in a structurally labile metabolically active free form [14] that probably is a protein precursor of amyloid [15–17]. *In vitro* at pH~7, free SAA solubilizes vesicles

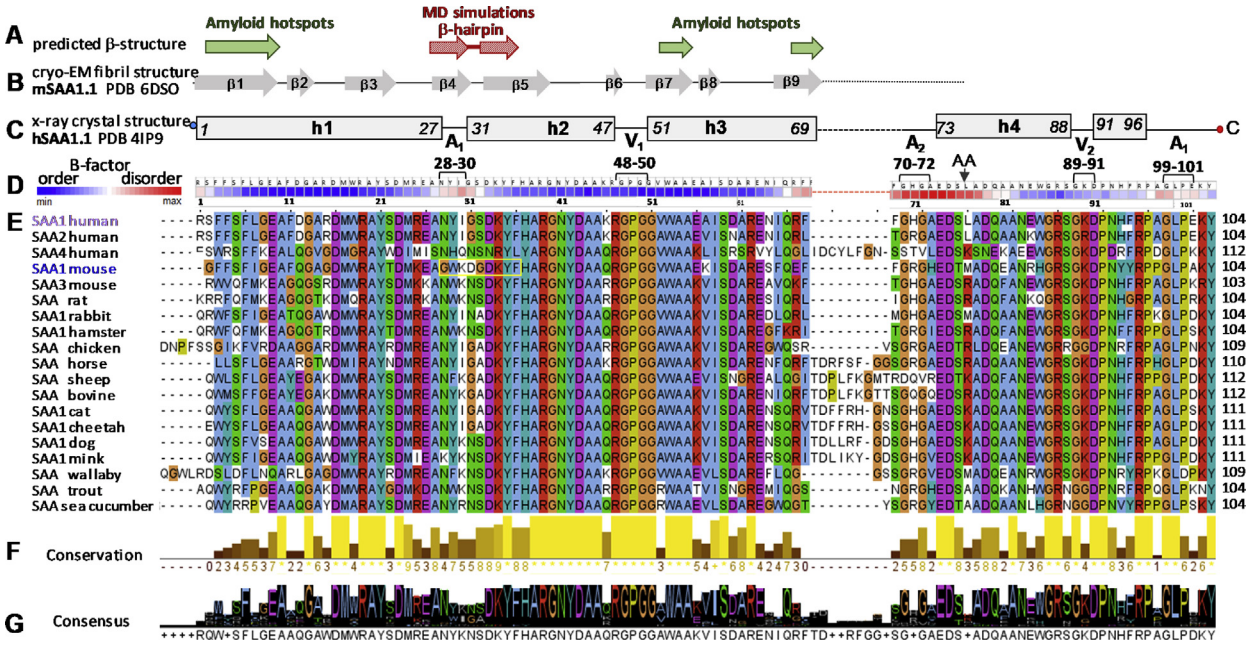

Fig. 1. Predicted and observed secondary structure and amino acid sequence conservation in the SAA protein family. The residue numbers correspond to human SAA1. (A) Predicted β-sheet structure. Green arrows show residue segments predicted to initiate β-aggregation in SAA, or "amyloid hotspots" [15]; brown arrows show the β-hairpin predicted by MD simulations of the current study. (B) Linear diagram shows β-sheets observed in the AA amyloid structure, derived from mSAA1.1 (PDB: 6DSO); arrows represent β-strands and lines are turns/loops [34]. (C) Linear diagram depicts secondary structure observed by x-ray crystallography (PDB 4IP9) in lipid-free hSAA1.1 [31]. Rectangles show α-helices h1-h4 and a 3/10 helix h'; first and last residue numbers in each helix are indicated. Lines show turn/coil regions; dashed line indicates the variable h3-h4 linker. Apices 1 and 2 (A_1, A_2) and vertices 1 and 2 (V_1, V_2) are indicated, along with their residue numbers (see Fig. 2 for detail). Residues numbering is according to human SAA1 that has an additional N-terminal Gly compared to murine SAA1. (D) Temperature factors of the Cα atoms from the crystal structure of hSAA1.1 (PDB: 4IP9); the B-factors are color-coding as shown, from low to high (blue to red). Similar B-factor distribution was observed in all nine symmetry-unrelated SAA molecules from the four available crystal structures of hSAA1 and mSAA3 (PDB: 4IP8, 4IP9, 4Q5G, 6PY0) in four different space groups; therefore, this B-factor distribution was determined by factors other than lattice contacts. Amino acids are shown for hSAA1. Black arrow shows the major cleavage site that generates AA fragment found in the *in vivo* deposits. (E) The conservation table lists amino acid sequences of 19 SAA proteins. The sequence alignment was performed using the Clustal Omega server [64], and the results were displayed using Jalview, http://www.jalview.org/ [65]. Conserved residues are color-coded: apolar (blue), polar (green), acidic (purple), basic (red), Pro (yellow), Gly (orange). Yellow box highlights the β-hairpin observed in our MD simulations of mSAA1. (F) Conservation plot shows more conserved residues in lighter colors; the bar height represents the number of tabulated SAA sequences, wherein each residue is conserved. (G) Consensus plot shows the predominant residues in each position.

containing diverse phospholipids, cholesterol, and their mixtures [17–23], the products of lipid oxidation [24], and lipophilic vitamin retinol [25,26]. Binding of diverse lipids suggests that SAA can act as a lipid scavenger. Moreover, *in vitro* SAA can spontaneously solubilize phospholipid bilayers to form HDL-size particles (8–10 nm) that are hydrolyzed by another acute-phase reactant, secretory phospholipase A_2. SAA also sequesters toxic products of lipolysis, compelling us to propose that SAA and secretory phospholipase A_2 act in synergy to remove cell membrane debris from the sites of injury [27]. In summary, compelling evidence indicates that lipids are the major functional ligands of SAA, which regulate its activity and metabolic fate, and that SAA preferentially binds to HDL-size particles *in vivo* or forms them *de novo* [27–29]. The current study establishes the structural basis for SAA-lipid interactions in such particles.

In addition to lipids, SAA binds various cell receptors involved in lipid homeostasis and host defense, including CD36, SR-BI, LOX1, RAGE, TLR2, and TLR4, along with other diverse ligands ([9,11,29] and references therein). Such promiscuous ligand binding, as well as amyloid formation, probably stem from the dynamic conformation of SAA [21,23]. In fact, SAA is an intrinsically disordered protein that is substantially unfolded at near-physiological conditions in the absence of bound ligands [30].

Remarkably, x-ray crystal structures of lipid-free human SAA isoform 1.1 (hSAA1.1) and murine SAA

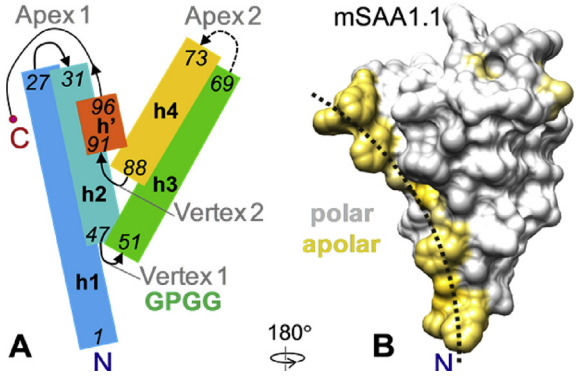

Fig. 2. SAA monomer x-ray crystal structure and model. (A) Cartoon representation of the SAA monomer based on the ~2.2 Å resolution x-ray crystal structures of hSAA1 and mSAA3 [25,26,31]. Rectangles show α-helices (h1, h2, h3, h4) and a 3/10 helix (h'), rainbow-colored from the N- to the C-terminus (blue to red). First and last residue numbers in each helix are in italics. Residue numbering is according to hSAA1. Two apices and two vertices are indicated. Dashed line shows a variable h3-h4 linker at the apex 2. (B) Space-filling model illustrating surface hydrophobicity of mSAA1 monomer. A homology model of mSAA1 was obtained using the crystal structure of hSAA1 (PDB ID 4IP9) and Swiss model software [66]. Hydrophobic residues are colored yellow. Dotted arc indicates a concave hydrophobic surface whose radius of curvature, r~4.5 nm, ideally fits the HDL surface curvature. Crystal structures of hSAA1 and mSAA3A show a similar hydrophobic surface [21].

isoform 3 (mSAA3) have been determined to ~2 Å resolution in four different crystal forms [25,26,31]. All forms present a similar Y-shaped helix bundle with ~75% helical content, comprised of α-helices h1 through h4 followed by a 3/10 helix h' (Fig. 2A). Hooper and colleagues noticed that the protein interior is polar, and proposed that this atypical fold has been evolutionally conserved to bind retinol [25]. The current study determines how the crystal structures relate to the partially disordered protein conformations in solution and in lipoproteins.

Previous studies using SAA truncations and antibody binding have implicated the N-terminal ~10 residues in lipid binding and self-association [18,31–33]. However, the deletion of these residues did not completely eliminate lipid binding, suggesting that other protein regions are involved. We observed that in the crystal structures, the two amphipathic α-helices, h1 and h3, form a large concave hydrophobic surface in SAA monomer (Fig. 2B) and proposed that this surface binds HDL and lipids [21]. Recent crystallographic studies supported this idea and showed that a hydrophobic pocket created by h1 and h3 in the well-ordered SAA oligomer binds retinol [26]. The current study combines experimental and computational approaches to elucidate the lipid-binding mechanism of this intrinsically disordered protein. The results provide key insights into the conformation of lipid-free SAA in solution (the structurally labile and metabolically active transient form that is the likely precursor of amyloid) and in model HDL-size lipoproteins (the major circulating form of SAA *in vivo*).

Results

HDX MS of lipid-free SAA at 5 °C reveals local trends that parallel the crystal structures

We used recombinant full-length murine SAA isoform 1 (mSAA1, or SAA for brevity); this major isoform binds HDL and forms amyloid *in vivo*. The residue numbering throughout this paper corresponds to human SAA1 that has an additional N-terminal Gly. The protein was obtained as described in Methods; the amino acid sequence marked "SAA1 mouse" is shown in Fig. 1E. The protein was characterized for self-association, secondary structure, and stability using gel electrophoresis, size-exclusion chromatography, mass spectrometry (MS), and circular dichroism (CD) spectroscopy (Figures S1, S2). Lipid-free mSAA1 was 25 ± 5% α-helical at 5 °C and unfolded upon heating to 25 °C with a midpoint T_m = 18 °C (Figure S2) [19]. Hydrogen-deuterium exchange (HDX) MS data were recorded as described in Methods using 0.5 mg/ml protein in standard buffer (10 mM sodium phosphate, pH 7.5). The HDX data summary and experimental conditions are reported in Table S1. Linear sequence coverage was 95–100% with ~5-fold redundancy (Figure S3), facilitating a rigorous analysis by HDX MS.

The HDX MS results at 5 °C revealed substantial variations in deuteration across the molecule, as shown in the deuterium uptake plots for representative regions (Fig. 3), and in the data summary for all regions (Fig. 4A, Supplemental dataset 1). Most regions from the N-terminal half of SAA, which contains h1, h2, and the N-terminal part of h3, showed relatively slow exchange, indicating high protection consistent with the presence of ordered structure. Except for the N-terminal portion of h4 discussed below, the rest of the molecule showed much lower protection from an exchange, especially in the C-terminal part of h3 and the C-terminal tail. Therefore, at 5 °C, the helical structure in free protein must be located mainly in its N-terminal half.

In spite of large differences in the α-helical content of free SAA in solution (~25% at 5 °C) and crystals (70–75%) [25,26,31], x-ray crystallography and HDX showed very similar trends in the local ordering of the helical and interhelical regions. In the crystals, helices h1 and the h2-h3 segment were substantially

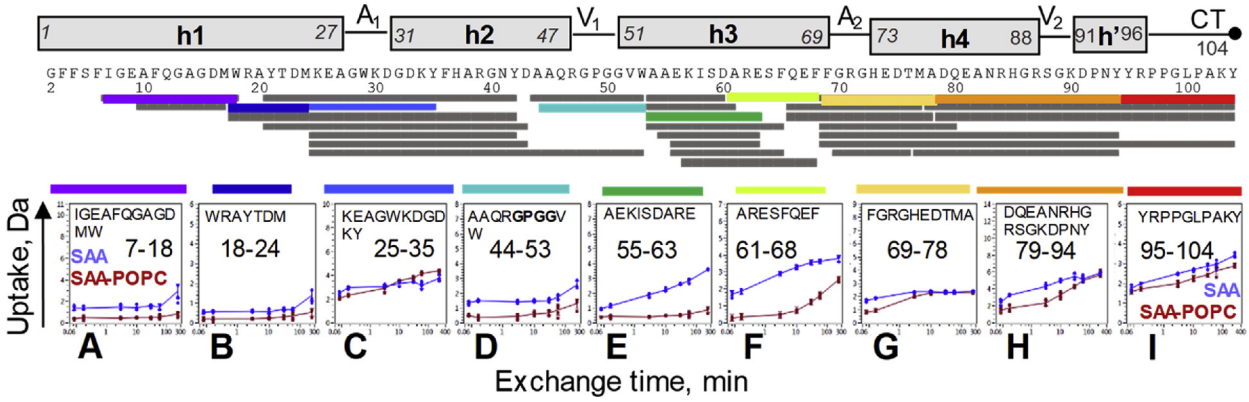

Fig. 3. Deuterium uptake plots for selected regions of lipid-free SAA (blue) and SAA-POPC (red). Error bars for individual time points represent the range for multiple charge states (varies per peptide) from the combined results of multiple replicates (described in Table S1 and in Methods). Residue numbers for representative peptides are indicated. Linear representation of the SAA secondary structure observed by crystallography is shown at the top. Apices 1 and 2 (A_1, A_2), vertices 1 and 2 (V_1, V_2), and the C-terminal tail (CT) are indicated; Fig. 2A shows their locations in the crystal structure. Peptide coverage map for lipid-free SAA and SAA-POPC at 5 °C is shown above the uptake plots. Each bar represents a peptic peptide fragment of SAA detected by MS. Selected fragments whose uptake plots are displayed are color-coded.

more ordered/less dynamic (had lower B-factors) than the C-terminal ~35 residues (Fig. 1D). This parallels the relative protection observed by HDX in these regions (Fig. 4A).

The four interhelical linkers observed in the crystal structures (Fig. 2A), including h1-h2 (apex 1), h2-h3 (vertex 1), h3-h4 (apex 2), and h4-h' (vertex 2), showed distinct HDX protection in solution. Notably, the h1-h2 linker region of free SAA, which is best represented by the peptide 25–35 (marked A_1 in Fig. 4A), showed more deuteration (less protection) than the adjacent segments from h1 and h2 at early deuterium-labeling times. The crystal structures also show the h1-h2 linker to be less ordered than its adjacent helices (Fig. 1C and D).

The h2-h3 linker (represented by peptides 44–53 and 45–53, marked V_1 in Fig. 4A) showed comparable or greater protection than the adjacent well-protected segments from h2 and h3. Similarly, the crystal structures showed uniformly low B-factors in h2, h3, and the h2-h3 linker (Fig. 1D), including the GPGG motif that formed a tight interhelical turn (Fig. 2A) [21]. Hence, despite its potential flexibility, the GPGG motif was well-ordered both in the crystals and in solution.

Unexpectedly, the h3-h4 linker region, which is also potentially flexible due to the presence of conserved G70 and G72, showed greater HDX protection in solution than the adjacent segments from h3 and h4. In our HDX MS analysis, this region (marked A_2 in Figs. 3 and 4) was best represented by peptides 69–78 and 70–76, which also contains the beginning of h4. The crystal structures showed an opposite trend; the h3-h4 linker, which forms apex 2, together with the beginning of h4, formed the least ordered region in SAA (Fig. 1D). Notably, the h3-h4 linker has variable length and composition in SAA proteins (Fig. 1E), and the beginning of h4 contains the major cleavage site after residue 76 that generates the N-terminal fragments found in AA amyloid deposits *in vivo* [3,34]. Therefore, high structural protection observed in this region by HDX MS was a surprise; MD simulations described below help explain this unexpected observation.

Finally, the h4-h' linker in residues 89–90 (contained within the peptide 79–94 and marked V_2 in Fig. 4A) showed slightly greater protection than its adjacent segments. This is consistent with the relatively well-ordered structure in this linker observed in the crystals (Fig. 1D), which forms vertex 2 packed against vertex 1 in the middle of the molecule (Fig. 2A). However, such packing requires ordered helices h4 and h', which is apparently not the case in solution, given the relatively high deuteration of residues in the C-terminal half of SAA. In free protein in solution, the C-terminal half lacks a stable helical structure. Nevertheless, substantial protection in vertex 2 observed by HDX, combined with lower but still meaningful protection in the rest of the C-terminal region of SAA (Fig. 4A), indicates that this region is not entirely disordered.

In summary, HDX results at 5 °C indicate that for free SAA in solution, most helical structure is located in the N-terminal half, while the C-terminal half is relatively disordered/flexible, except for the beginning of h4. Importantly, despite the large difference in the helical content of free SAA in solution (25–30% α-helix at 5 °C) and in the crystal (70–75%), HDX of free SAA at 5 °C and x-ray crystallography show similar trends in the local

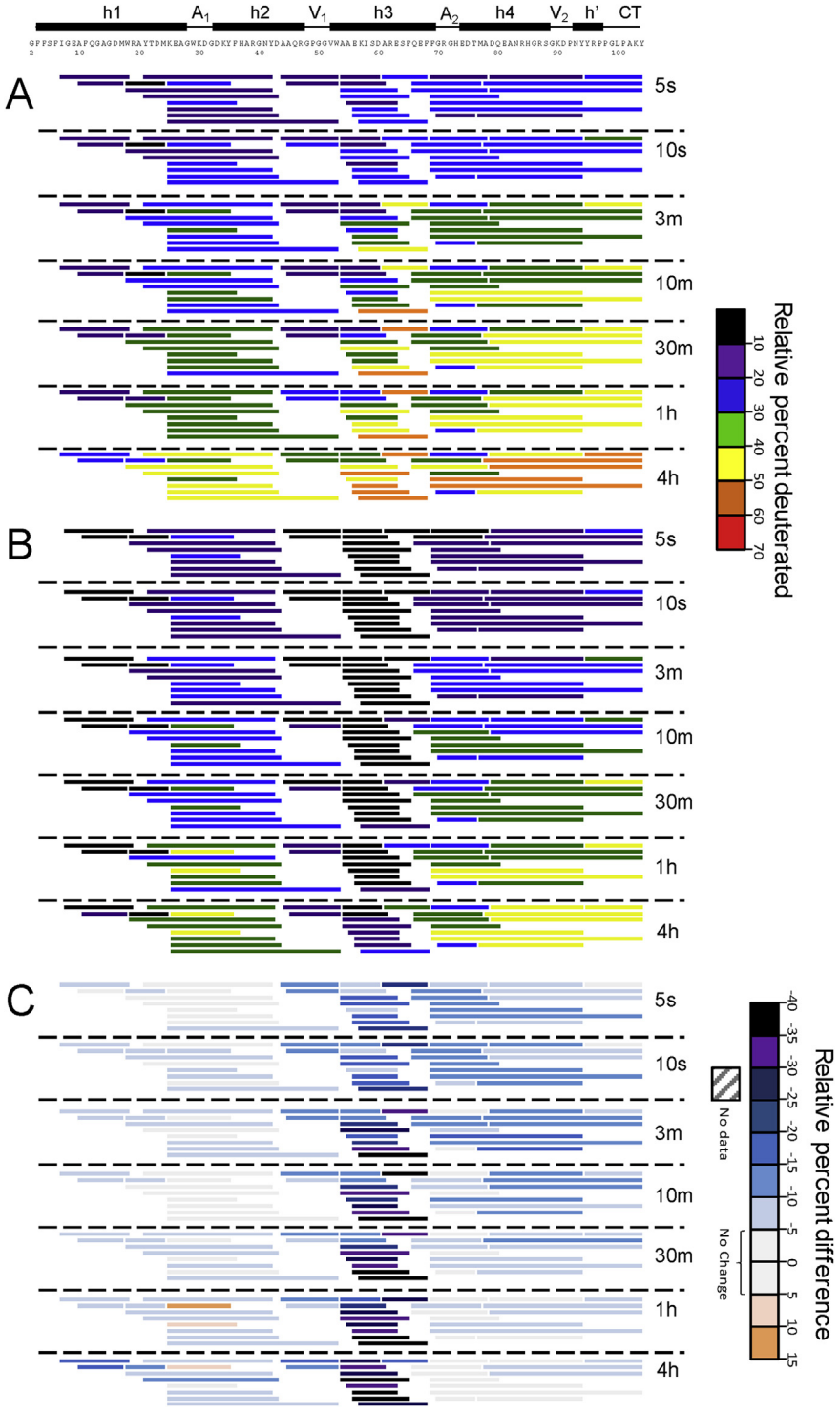

Fig. 4. Relative deuterium incorporation at 5 °C of all peptides in lipid-free SAA (A), in SAA-POPC (B), and their difference (C) where subtraction was performed as $D_{SAA\text{-}POPC} - D_{SAA}$. The relative percent deuteration scale for panels A and B is used to color each peptide from black/violet (low uptake, high structural protection) to red (high uptake, low structural protection). The deuteration difference scale for panel C indicates less deuteration (negative numbers and colors) in SAA-POPC. Similar data at 15 °C and 25 °C are shown in Figures S4, S5.

ordering of α-helical and linker regions. Consequently, the x-ray crystal structures depict the key aspects of the solution conformation of free SAA. The only discrepancy between the local structural ordering in solution and in the crystals was observed in the h3-h4 linker region at apex 2 (Fig. 4A), suggesting that the local solution conformation near this apex deviates from the crystal structure.

Insights from HDX MS analysis of free SAA at 15 °C and 25 °C

To analyze the solution conformation of SAA at temperatures closer to physiological conditions and to monitor protein unfolding, HDX MS was performed at 15 °C where free SAA is in the middle of thermal unfolding, and at 25 °C where thermal unfolding is nearly complete (Figure S2). For any protein, the temperature can influence HDX both because the intrinsic rates of exchange go up with temperature [35] and because the protein becomes more dynamic/flexible—and therefore, more easily deuterated—as temperature increases. While one cannot use HDX to compare the structural effects of exchange at two temperatures without compensating for changes in the intrinsic HDX rates, one can compare *differences* in exchange between two states at one temperature (*e.g.* 5 °C lipid-free vs 5 °C lipid-bound) to differences in exchange at another temperature (*e.g.* 15 °C).

The results in Fig. 4, S4 and S5 showed that HDX was progressively greater, going from 5 °C to 25 °C. When the intrinsic rates of exchange were considered, by mathematically adjusting the measured exchange at 5 °C to what it would be at 15 °C and 25 °C, or by adjusting the measured exchange at 15 °C and 25 °C to what it would be at 5 °C (see Supplemental Dataset 1), calculated exchange was found to be slower at 15 °C and 25 °C than could be explained by temperature correction alone; that is, SAA was more protected at 15 °C and 25 °C than one would predict, mathematically based on the 5 °C HDX data. This makes sense in light of the CD melting curves (Figure S2), which show that SAA is partially (at 15 °C) or totally (at 25 °C) unfolded, which may influence its oligomerization (see below). HDX was progressively greater, particularly in the h2-h3 region, suggesting its unfolding. In free SAA at 25 °C, most regions showed little protection (Figure S5 A), consistent with the CD results indicating decreased helical structure (Figure S2). The only regions retaining substantial protection from deuteration at 25 °C were (i) residues 7–35, which encompass parts of h1, h2 and the h1-h2 linker at apex 1, and (ii) residues 69–80, which encompass the h3-h4 linker and the beginning of h4 at apex 2. Consequently, high structural protection in these two regions in solution was consistently observed at 5–25 °C, *i. e.* both below and above thermal unfolding of free SAA. The structural basis for this local protection emerges from our MD simulations described below.

A caveat in our experimental analysis of free SAA is its propensity to form oligomers of various sizes in a broad range of solvent conditions and temperatures [20,30,36] and references therein), including those used in our HDX experiments (Figure S1). Since the N-terminal end of h1 is implicated in self-association of free SAA in solution [30,33], this may contribute to high protection observed in h1 by HDX (Fig. 4A). However, since SAA self-association competes with lipid binding at pH~7 [16,21,33], it is not expected to significantly influence our HDX MS analysis of SAA-POPC complexes. In fact, binding to lipids stabilizes the structure of SAA, which likely makes it less prone to aggregation. This hypothesis is directly supported by the HDX results for SAA-POPC, as described next.

HDX MS analysis of SAA-POPC complexes at 5–25 °C

SAA-POPC particles differing in size from ~10 nm to ~20 nm were reconstituted using 1:10, 1:30, or 1:80 protein : lipid molar ratios, as described previously [29]; all particles showed similar secondary structure, thermal stability, and intrinsic Trp fluorescence that reports on SAA-lipid interactions. HDX MS analysis of SAA-POPC in 1:10, 1:30, or 1:80 particles showed that deuterium uptake plots were identical for the particles of different sizes (Figure S6), suggesting a similar protein conformation.

For detailed HDX studies, we selected 1:10 particles, henceforth termed SAA-POPC, which showed the highest temporal stability and were 8–10 nm in size like HDL [29]. The structure and stability of these SAA-POPC particles were characterized by gel filtration and CD spectroscopy (Figures S1, S2). HDX SAA-POPC was measured at 5 °C and 15 °C (Fig. 3 and 4B), and 25 °C (Figure S4 and Supplemental dataset 1). As described above for free SAA, HDX at higher temperatures would be expected to be faster due to the intrinsic rates of exchange. In fact, the results showed that, while the overall deuteration rate progressively increased from 5 to 25 °C, the site-specific trends remained invariant (panel B in Fig. 4, S4, and S5). This was in line with the CD data showing that the protein conformation in SAA-POPC remained invariant upon heating from 5 to 25 °C (Figure S2). At all temperatures, the greatest protection in SAA-POPC was detected in two segments, one containing the central part of h1 (residues 7–24) and the other extending from the C-terminal end of h2 to the end of h3 (panel B in Fig. 4, S4 and S5). Consequently, these two segments contained the most helical structures in SAA-POPC.

Comparison of HDX MS data of free SAA and SAA-POPC reveals the lipid-binding site

A comparison of HDX data for SAA-POPC and free SAA showed that the structural protection increased nonuniformly across the protein molecule upon lipid binding. At 5 °C, the greatest increase was observed in the central and C-terminal part of h3 that showed low protection in free SAA but very high protection in SAA-POPC (Fig. 3E and F; Fig. 4). At 15 °C and 25 °C, when progressive helical unfolding was observed by CD spectroscopy in free SAA but not in SAA-POPC (Figure S2), the difference between SAA-POPC and free SAA was further amplified (Figures S4, S5; Supplemental file 1). These results suggest that the large lipid-induced increase in protection of h3 observed by HDX at 5–25 °C reflects coupled helical folding and lipid binding. Lipid binding stabilizes the helices greatly; h3 unfolds upon heating free SAA from 5 to 25 °C but remains helical on POPC.

The interhelical linkers in SAA-POPC, like in free SAA, showed distinct trends in local protection from HDX at all temperatures explored (Fig. 3; panel B in Fig. 4, S4 and S5). Interestingly, the h1-h2 linker (A_1), which in free SAA showed more exchange (less protection) than the adjacent segments from h1 and h2, showed even more exchange (lower protection) than the adjacent segments in SAA-POPC. Another unexpected finding was that the h1-h2 linker consistently showed a meaningful lipid-induced deprotection (rather than protection) at all temperatures explored (pink regions in panels C of Fig. 4, S4 and S5). These results suggest that a more ordered solution conformation in the h1-h2 linker forms in free protein compared to SAA-POPC. The nature of this ordered conformation emerges below from our MD simulations.

Furthermore, lipid binding increased the protection in the h2-h3 linker (V_1) at 5 °C (Figs. 3D and 4C), and this increase was greatly amplified at higher temperatures. Other protein regions showed small lipid-induced changes in protection at 5–25 °C (Fig. 4, S4, S5).

Taken together, these results revealed that both helical and interhelical regions observed by x-ray crystallography show distinct structural protection in free protein in solution, as compared to SAA-POPC. Therefore, the key aspects of the monomer fold seen in the SAA crystal structure must be retained in solution and on the lipid. Interestingly, h1-h2 linker showed more protection in free SAA, as compared to SAA-POPC at 5–25 °C (Fig. 4, S4, S5), although free SAA but not SAA-POPC underwent helical unfolding at the higher temperatures (Figure S2). A likely origin of this paradoxical observation emerges below in our MD simulations. Notably, of all linkers, the h2-h3 turn at vertex 1 showed the largest increase in protection upon lipid binding at 5–25 °C (Fig. 3E and F; panel C in Fig. 4, S4 and S5). The structural basis for this observation is described below.

HDX suggests lipid-induced conformational selection at vertex 1

The mass spectra for each peptic fragment were analyzed for the presence of EX1 and EX2 kinetics, the two kinetic extremes in proteins that are easily observed by HDX MS [37,38]. In EX2, which is predominant in well-folded globular proteins, local refolding is faster than the HDX reaction, and progressive deuteration occurs upon multiple unfolding and refolding events. EX2 manifests itself as a unimodal spectrum with an isotope distribution that gradually shifts toward a higher mass as a function of deuteration time. In EX1, the deuteration occurs after a cooperative or coordinated unfolding event where local refolding is slower than HDX. EX1 manifests itself as a bimodal spectral distribution (when the alternative conformations are separated on the m/z scale) or as spectral broadening (when the two populations are close in m/z), with the lower-mass peak corresponding to the protected conformation and higher-mass peak to the unprotected one. EX1 generally indicates the coexistence of alternative conformations.

At 5 °C, most short peptides in free SAA and in SAA-POPC showed EX2 exchange behavior. However, in free SAA, all peptides encompassing the middle of h1 (e. g. peptide 7–18) and a region from the middle of h2 to the middle of h3 (e. g. peptides 45–53 and 54–65) showed EX1 (Fig. 5). In SAA-POPC, the mass spectra showed a dominant lower-mass peak representing a large population of well-protected species, while in free SAA, the spectra also showed a higher-mass peak representing the unprotected species (Fig. 5). At 15 °C, which is close to T_m~18 °C of free SAA (Figure S2), EX1 in these regions of free protein was even more obvious, with two well-resolved peaks suggesting high populations of at least two distinct conformations, one poorly protected (fast exchange) and another more protected (slow exchange) (Figure S7). Upon temperature increase from 5 to 15 °C, in free SAA there was a large shift from a highly protected to the poorly protected conformation (Fig. 5, S7), but in SAA-POPC at 15 °C only the highly protected conformation was observed (Figure S7). These trends continued at 25 °C: in free SAA, HDX MS showed further population shift toward the poorly protected conformation (Figure S7), while CD data showed a largely unfolded helical structure (Figure S2). At all temperatures explored, the highly protected conformation was selectively stabilized in SAA-POPC (Fig. 5, S7).

Importantly, segments from h1 and h2-h3 that clearly showed EX1 for free SAA in solution pack

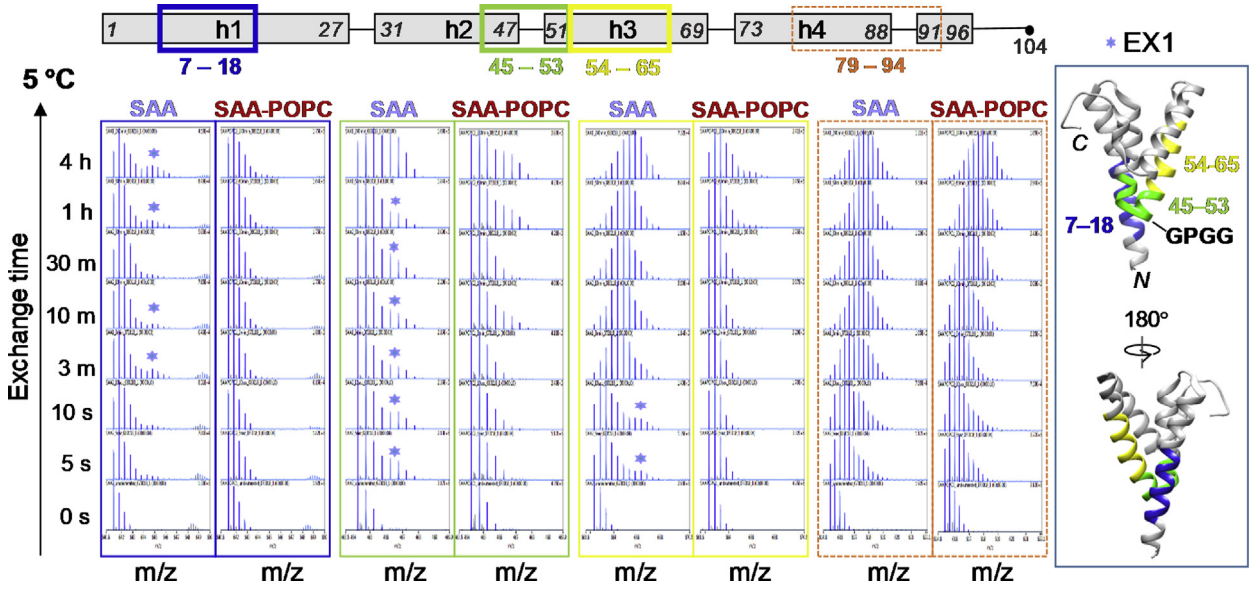

Fig. 5. Mass spectra of selected peptides that display EX1 kinetics at 5 °C. Other peptides that overlap those shown here (see Fig. 3 and 4) also displayed EX1 kinetics. Spectra are shown for free SAA (left of each pair) and for SAA-POPC (right of each pair) as a function of the exchange time for peptides 7-18 (blue boxes), 45–53 (green boxes), 54–65 (yellow boxes). The regions showing EX1 in free SAA, color-coded in blue (residues 7–18), green (45–53), and yellow (54–65). Each of these peptides is indicated in the linear protein model (top) and is mapped on the crystal structure (far right). Stars indicate spectra that clearly show two peaks characteristic of EX1 regime. Spectra for a representative peptide showing only EX2 (residues 79–94, orange boxes) are shown for comparison. Figure S7 shows similar data of selected peptides that display EX1 kinetics at 15 °C and at 25 °C.

against each other at vertex 1 in the crystal structure (Fig. 5, right), which helps explain the coupled conformations of these segments in solution. We conclude that in free SAA at 5–25 °C, the region around vertex 1 displays at least two distinct conformations. During the thermal unfolding of free SAA, the poorly protected conformation becomes predominant at the expense of the highly protected conformation (Fig. 5, S7). The latter is selectively stabilized upon lipid binding (Fig. 5, S7), leading to a lipid-induced increase in the overall structural protection in h1 and h2-h3 region observed at all temperatures explored (Fig. 4, S4, S5). We propose that these distinct conformations reflect alternative states of the GPGG motif, one unfolded as expected of this Gly-rich motif, and the other one well-folded and perhaps resembling vertex 1 packing in the crystal structure.

MD simulations of SAA monomer in solution and on the POPC micelle

To gain additional insights into the SAA conformation in solution and on the lipid surface, MD simulations were performed as described in Methods and illustrated in Figure S8. The starting configuration of full-length mSAA1 monomer, termed SAA_{68}, was 68% α-helical and was modeled based on the x-ray crystal structure of hSAA1 (Figure S9 C). To promote helical unfolding, and thereby, approximate the solution conformation of the lipid-free protein, SAA_{68} was simulated at 370 K for 3.8 μs. We observed a progressive unraveling of h4, h2, N- and C-terminal ends of h1, and the C-terminal part of h3 (Fig. 6). This result was supported by an experiment, as similar regions in free SAA showed low protection from HDX (panel A in Fig. 4, S4 and S5), except for the N-terminal end of h1 the protection of which was probably influenced by the protein self-association.

During the last microsecond of the high-temperature trajectory, the average helical content was ~30%, approaching that estimated from the CD spectra of free SAA at 5 °C. This last microsecond was used to extract representative structures to assess the protein conformational ensemble at ambient temperatures. Three structures, collectively termed SAA_{30}, were extracted based on a clustering analysis; each structure was simulated at 310 K, either lipid-free (denoted SAA_{R1} – SAA_{R3}) or on a POPC micelle (denoted SAA-$POPC_{R1}$ – SAA-$POPC_{R3}$) as described in Methods. Figure S10 shows the time evolution for the secondary structure in each simulation.

Fig. 7A illustrates external H-bonding between the main chain nitrogens of SAA and water molecules in

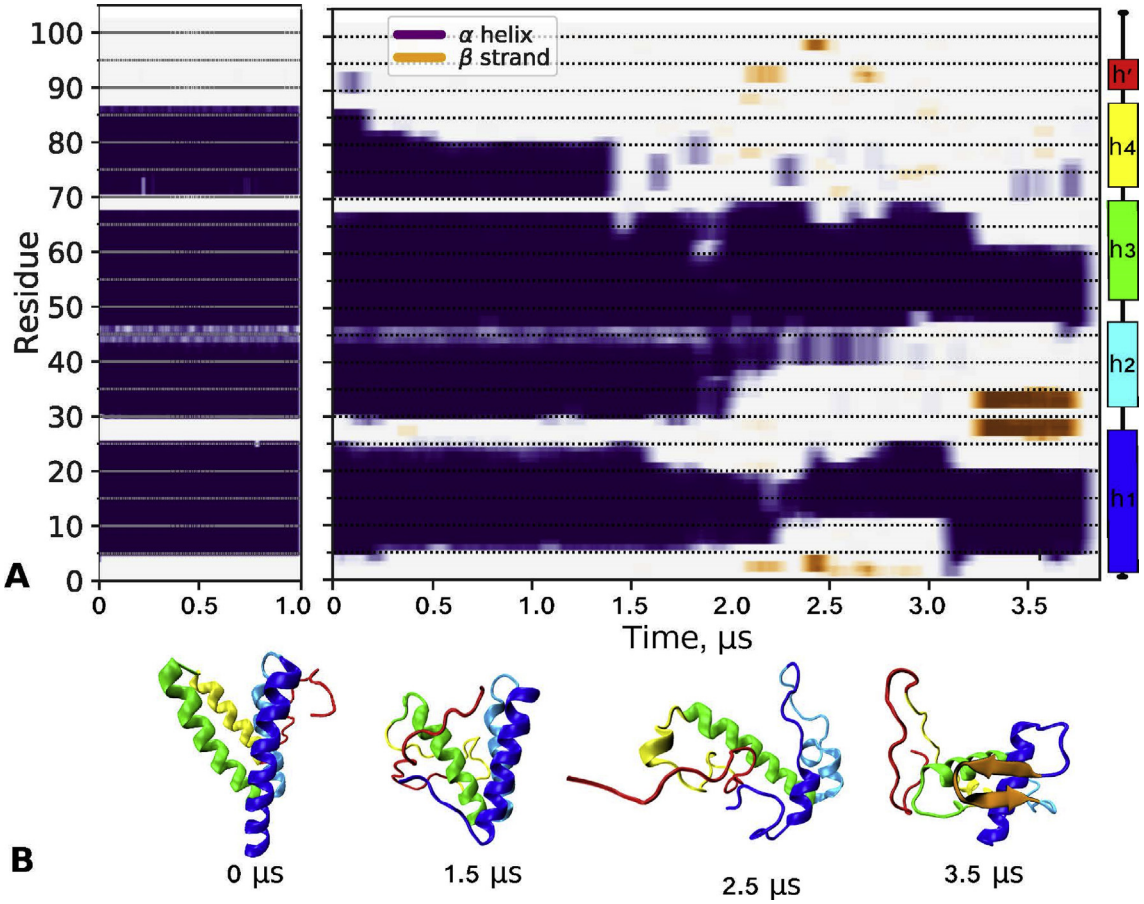

Fig. 6. Low- and high-temperature simulations of lipid-free SAA monomer in solution. The starting model, denoted SAA_{68}, was obtained from the x-ray crystal structure of hSAA1 (PDB ID: 4IP8), as shown in Figure S9. The structure was simulated at 310 K for 1 μs and at 370 K for 3.8 μs as described in Methods. (A) Time evolution of the secondary structure showing α-helices (purple/blue) and β-sheets (orange/brown) over the simulation trajectory at 310 K (left) and 370 K (right panel). The remaining structure (off-white) was turn/coil. Linear secondary structure model based on the hSAA1 crystal structure is color-coded. (B) Representative molecular structures at indicated simulation times from the 370 K trajectory, from 0 μs (SAA_{68}) to 3.5 μs. The orientation of h1 is similar in all figures. Color-coding: h1 (blue), h2 (teal), h3 (green), residue segment 70−104 (red), and β-sheet (orange).

SAA_{68} and SAA_{30}, averaged over R1 − R3 runs, and Figure S11A shows such external H-bonding for individual runs of SAA_{30}. The results consistently show that, unlike the rest of the molecule, the central part of h1 (residues 6−24), as well as the h2-h3 linker and most of h3 (residues 50−64) except for its C-terminal part, are protected from the main chain H-bonding with water. This result agrees with HDX MS showing high protection from HDX in h1 and in the N-terminal half of h3 in free SAA (panel A in Fig. 4, S4 and S5).

Fig. 7B depicts the secondary structural propensity in SAA_{R1} − SAA_{R3} and SAA-$POPC_{R1}$ − SAA-$POPC_{R3}$. Lipid-free SAA shows two major highly α-helical regions: the central part of h1 and the residue segment encompassing the h2-h3 linker and most of h3 except for its C-terminal part. Our MD simulations suggest that experimentally observed high protection from the exchange in these regions of free SAA results from their stable helical structure. Moreover, MD simulations predict substantial helicity in the h3-h4 linker and at the beginning of h4 spanning residues 71−77 (Fig. 7B). This helps explain why this region shows relatively high protection from the exchange (e.g. peptide 69−78 in Figs. 3G and 4A, S4A, and S5A), although in all available x-ray crystal structures this variable region is substantially disordered/dynamic (Fig. 1D).

Unlike free protein whose average secondary structural content changed little in simulations of SAA_{30} at 310 K, the helical content in similar simulations of SAA-POPC increased, suggesting lipid-induced helical stabilization (Fig. 7). A clear increase was seen in the h2-h3 linker and in the C-terminal part of h3, which regained complete helicity in SAA-$POPC_{R3}$. This trend agreed with the HDX

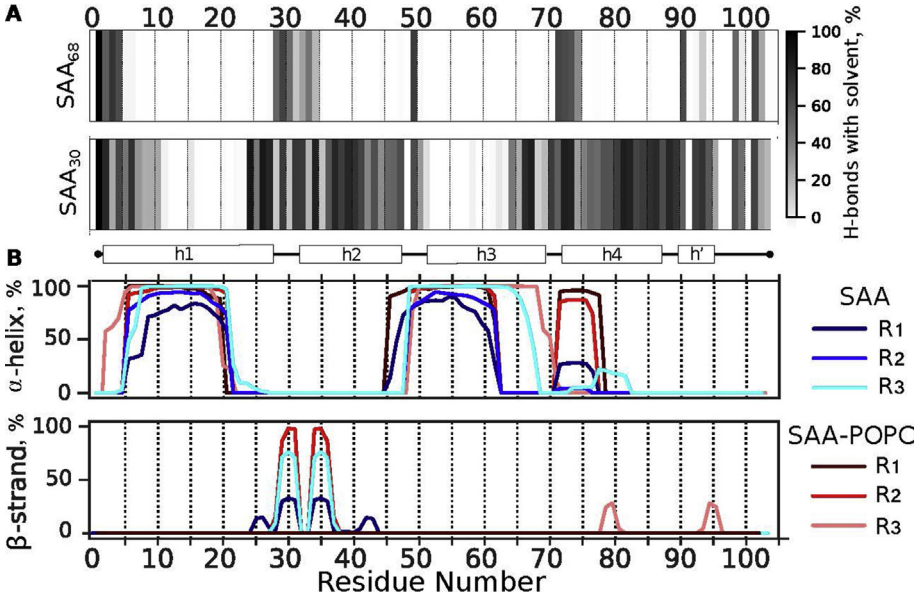

Fig. 7. Main chain hydrogen bonding and secondary structure in SAA monomer in solution. Three representative structures collectively termed SAA_{30}, which were extracted from the last 1 μs of the 370 K trajectory (shown in Fig. 6A), were equilibrated at 310 K in the absence (SAA) or presence of a POPC micelle (SAA-POPC) for 5 or 10 μs, respectively. The resulting models, denoted R_1-R_3, are reported. (A) Hydrogen bonding of the protein main chain nitrogens to water molecules. Fraction of frames showing H-bonds with water is plotted versus residue number; darker colors indicate greater H-bonding probability. The plots represent an average of R_1-R_3 models; the results for individual models and their 3D structures are shown in Figure S11. Similar data for the starting model, SAA_{68}, are shown for comparison (top panel). (B) Location of the α-helices and β-strands in the primary sequence of SAA and SAA-POPC is shown for R1-R3 models. Individual replicates are color-coded.

data showing a large lipid-induced increase in the structural protection of the C-terminal part of h3 upon POPC binding at all temperatures explored (Fig. 4C, S4C, S5C). As the helical content in our simulations of SAA-$POPC_{R1}$ – SAA-$POPC_{R3}$ has not yet reached the ~50% level observed in SAA-POPC complexes by CD spectroscopy, a direct quantitative comparison of computational and experimental results was not possible. However, the trends predicted in our MD simulations were validated by the CD and HDX MS data. Taken together, these data demonstrate that interactions with the lipid surface stabilized the helical structure throughout the SAA molecule and induced helical folding in the C-terminal part of h3.

To identify protein regions that interact with the POPC surface, SAA_{68} was randomly oriented 5 nm away from the micelle surface and allowed to diffuse and interact with a preformed POPC micelle at 310 K for 1 μs. In the initial orientation, helices h1 and h3 were not facing the micelle. During the first ~50 ns of the simulation, the protein explored various orientations with respect to the micelle before converging to a stable orientation after ~90 ns (Fig. 8A). In this orientation, the protein contacts with the phospholipid head groups and acyl chains were formed largely by helices h1 and h3, with minimal contributions from h2 and no contributions from residues 70–104 (Fig. 8B). Fig. 8C illustrates the protein orientation on the micelle; the protein-lipid contacts mainly involve the hydrophobic faces of h1 and h3. This result, combined with our comparative HDX studies of SAA and SAA-POPC (Fig. 4, S4, S5, 5, and S7), supports the conjecture that the hydrophobic faces of h1 and h3 form the lipid-binding site in SAA.

The h1-h2 linker region can form a β-hairpin

Although the SAA crystal structures contain no β-sheet, our MD simulations predicted an unexpected β-hairpin with β-strands in residues 28–30 and 33–35 encompassing the h1-h2 linker and the beginning of h2 (Fig. 7B, S10-S12). The β-hairpin first formed in the 370 K simulations (Fig. 6) and was partially retained at 310 K in SAA_{R1}, SAA_{R2}, and SAA-$POPC_{R2}$ (Figure S10). Structural analysis of SAA_{R1} and SAA_{R2} suggests a network of fluctuating interactions, including aromatic ring stacking W29–W35 and W29–F36, a cation-π interaction between K30–Y35, the formation of ion pairs D33-K34 and K30-D33, and charge-dipole interactions, e.g. K30-G32 carbonyl oxygen (Figure S12). The combined effect of these and other weak interactions confers marginal stability to

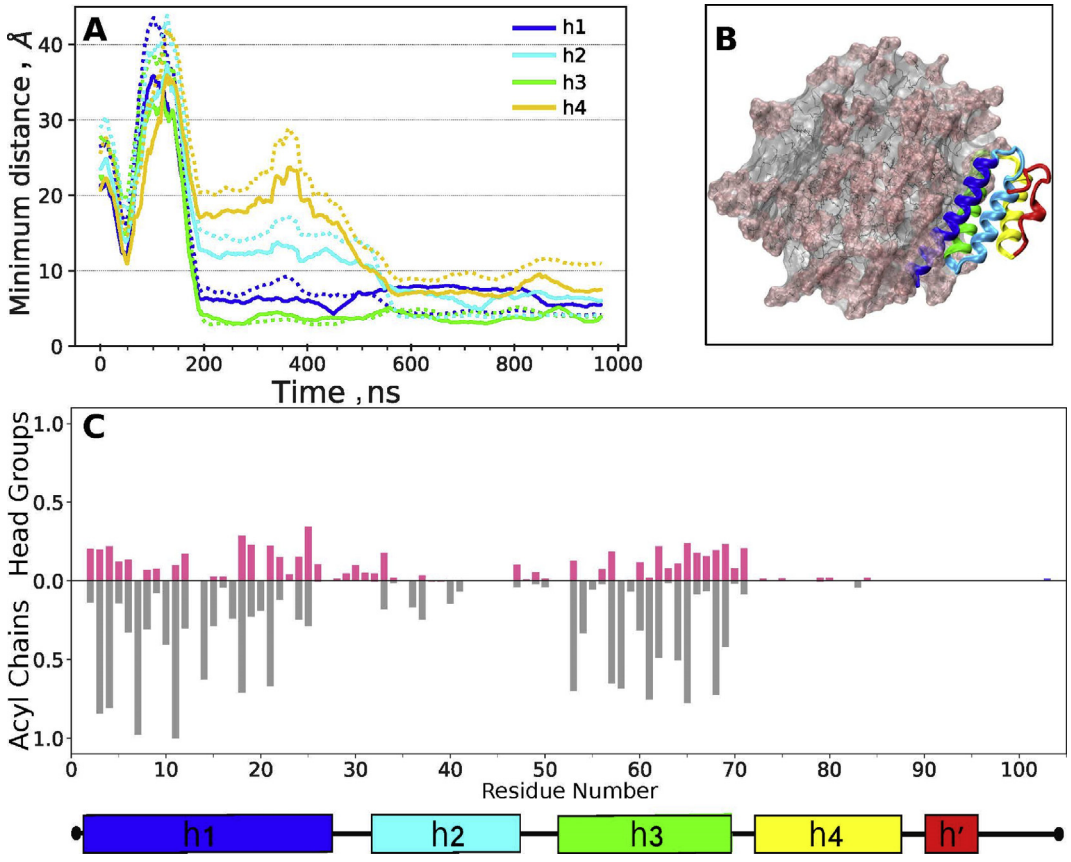

Fig. 8. Protein-lipid contacts in SAA-POPC$_{68}$ model. SAA$_{68}$ was oriented randomly in respect to the POPC micelle containing 72 lipid molecules, the system was simulated at 310 K for 1 μs (for detail see flowchart in Figure S8), and the last 0.5 μs of the trajectory were used for analysis. (A) Average protein-lipid distances are plotted as a function of simulation time for individual SAA helices (color coded). Solid lines show distances involving phospholipid head groups, and dotted lines those involving acyl chains. (B) Final configuration of the SAA-POPC$_{68}$ system. Protein ribbon diagram shows h1 (blue), h2 (teal), h3 (green), h4 (yellow) and residue segment 70–104 (red). POPC head groups are in pink and acyl chains in grey. (C) Fraction of frames showing SAA contacts with the POPC head groups (pink) and acyl chains (grey) per residue. A contact is defined as lipid atoms within 5 Å of protein atoms. Average results from R_1-R_3 simulations are shown.

the observed β-hairpin. The nascent formation of the β-hairpin helps explain why peptide 25–35 in free SAA is better protected from HDX than its adjacent segments (Fig. 4A), although in the crystal structure this region has higher B-factors than the adjacent segments (Fig. 1D). Moreover, peptide 25–35 is the only region showing greater protection from the exchange in free SAA, as compared to SAA-POPC (orange in Fig. 4C, S4C, S5C). This experimental observation suggests that the β-hairpin is more likely to form in free SAA than in SAA-POPC.

Additional support for β-sheet formation in this region comes from the fibril structure of mSAA1 determined by cryo-electron microscopy [34]. Strands β4 and β5 in this structure overlap the β-hairpin strands predicted in our simulations (Fig. 1A and B). Moreover, a sharp bend between β4 and β5 at residues G32, D33 observed in the fiber structure overlaps the tight turn in the β–hairpin seen in SAA$_{R1}$ and SAA$_{R2}$ (Figures S10, S12).

In conclusion, our MD simulations and HDX MS data suggest that residues 27–35 can form a β-hairpin in mSAA1 monomer, while cryo-electron microscopy shows that similar β-strands are retained in amyloid fibrils of this protein. Therefore, this β-hairpin may represent a previously unknown misfolding intermediate on the pathway to amyloid formation.

Discussion

Crystal structures depict key aspects of the solution conformations of SAA and SAA-POPC

This study reports solution conformations of SAA ligand-free and in model HDL-size lipoproteins. It

establishes the structural basis for understanding how this intrinsically disordered protein binds lipids, and proposes an early step in the amyloidogenic α-helix to β-sheet transition in mSAA1 monomer. Our studies of mSAA1 free in solution or in SAA-POPC complexes agree in remarkable detail with the crystal structures of lipid-free hSAA1 and mSAA3, but also reveal important differences. Structural protection determined by HDX MS in free SAA and in SAA-POPC (Fig. 4) shows local trends similar to those in the crystallographic B-factors (Fig. 1D). The sole exception is the variable h3-h4 linker discussed below. This similarity was unexpected given large differences in the α-helical content of free SAA (~25% at 5 °C, <10% at 25 °C), SAA-POPC (~50% α-helix at 5−25 °C) (Figure S2), and the crystals (~75% α-helix). We conclude that the crystal structures depict essential aspects of the local conformation of SAA free in solution and bound to lipoproteins. Therefore, the crystal structure serves as a useful starting model for MD simulations, which provide additional insights into the solution conformation of free SAA, its interactions with the lipid surface, and its misfolding and formation of β-structure.

Helical structure in the N- and C-terminal regions

Previous amino-acid sequence analyses predicted that residues 1−70 contain the most stable helical structure in SAA [21,39]. Our experiments and simulations verify this prediction and show that in free SAA in solution, most helices are located in two segments, one including a large part of h1 and the other spanning from the end of h2 to the middle of h3. These segments show the greatest protection from HDX in free protein at 5 °C (Fig. 4A) and form particularly stable helices in MD simulations (Figs. 6 and 7). In the crystal structure, these segments are packed together at vertex 1 (Figs. 2 and 5), perhaps nucleating the native fold.

Unlike the N-terminal region, most of the C-terminal third of SAA lacks a stable secondary structure free in solution and on POPC; the only exception is the h3-h4 linker and the beginning of h4 at apex 2 (Fig. 4, S4, S5, Fig. 7B). Unexpectedly, both free SAA and SAA-POPC show relatively high HDX protection in peptides 69−78 and 70−76 encompassing apex 2 region (A_2 in Fig. 3G and 4A, S1A, S2A). In contrast, the crystal structures show high B-factors in this variable region (Fig. 1D). MD simulations reveal a likely basis for this discrepancy and predict high helicity in the linker residues 71−77 (RGHEDTM in mSAA1) in free protein and, particularly, in SAA-POPC, while the adjacent segments are unfolded (Fig. 7B). This helix is not expected to block the cleavage at the 76−77 junction to release the major AA fragment found in amyloid fibrils *in vivo*. Direct observation of this short helix and its functional role remain to be determined; this and other conclusions from our MD simulations remain to be verified in future studies. We speculate that such an α-helix may provide a recognition motif for cell receptors and other ligands that are implicated in binding SAA via its C-terminal ~30 residues [21]. It is possible that two strictly conserved acidic residues from this short helix, E74 and D75, attract the electropositive ligand-binding site in cell receptors, such as CD36, LOX-1, or SR-BI [40,41], facilitating SAA-receptor interactions.

Amphipathic α-helices h1 and h3 form an evolutionally conserved lipid-binding site

Our results revealed that POPC binding leads to increased protection from HDX across the SAA molecule, most strikingly in the C-terminal half of h3 that shows poor protection in the free protein but high protection in SAA-POPC (Fig. 3E and F; Fig. 4, S4, S5). This parallels increased helical content in SAA-POPC observed by CD spectroscopy (Figure S2). MD simulations support the observation that, while the helical structure across the SAA molecule increases upon POPC binding, the most substantial increase occurs in the C-terminal part of h3, which is unfolded in free SAA in solution but acquires α-helical structure in SAA-POPC (Fig. 7). Consequently, lipid binding induces helical folding in the C-terminal part of h3.

SAA-POPC shows the greatest protection from HDX in h1, h2-h3 linker and h3 (Fig. 3E and F; 4B; S4B; S5B). In free SAA, parts of h1 and h2-h3 segments show on average relatively high protection from HDX at 5 °C (Fig. 4A) but display alternative conformations differing in protection, as indicated by the EX1 exchange kinetics (Fig. 5, S7). By contrast, in SAA-POPC, this region shifts toward a highly protected conformation, suggesting its involvement in lipid binding (Fig. 5, S7). Moreover, MD simulations of SAA_{68} in the presence of a POPC micelle suggest that the amphipathic helices h1 and h3 directly interact with the lipid via their hydrophobic faces (Fig. 8). Additional evidence for lipid binding via these helices comes from the intrinsic fluorescence of the three Trp in mSAA1, which are located in the hydrophobic faces of h1 (W18) and h3 (W52) or in the h1-h2 linker (W29). A blue shift in the wavelength of maximal emission indicates that these tryptophans shift from a largely aqueous to a largely apolar environment upon POPC binding [29]. These findings, taken together, clearly show that the lipid-binding site in SAA contains both h1 and h3, and not just the N-terminal end of h1 as previously thought. Moreover, the hydrophobic cavity in SAA oligomer formed by h1 and h3 was recently shown to bind retinol [26]. These findings substantiate the idea that this site binds diverse apolar ligands of SAA [21].

Importantly, in the crystal structures, the N-terminal and central parts of h1, as well as the central and C-terminal parts of h3 in SAA monomer, form a concave hydrophobic face that optimally fits the HDL surface curvature (Fig. 2B). This suggests a structural basis for the preferential binding of SAA to HDL, which is its major plasma carrier [21]. The current study supports this conjecture and also establishes the structural basis for *de novo* formation of HDL-size particles by SAA. This is particularly important as sequestering unprotected lipids and their degradation products into nanoparticles is proposed to be a major evolutionally conserved function of SAA [27].

Interestingly, the protection from HDX observed in SAA-POPC parallels the evolutional conservation in the SAA protein family. The h2-h3 residue segment (Fig. 1F and G), the packing of which against h1 is necessary to form the concave hydrophobic lipid-binding face (Fig. 2), is particularly highly conserved. This conservation parallels high protection from the exchange of the h2-h3 segment observed in SAA-POPC at 5–25 °C (Fig. 4B, S4B, S5B). This parallel compels us to postulate that the amino acid sequence encoding for the unique molecular fold of SAA has been evolutionally conserved to encapsulate lipids into self-assembled nanoparticles.

Structural and functional roles of the N- and C-terminal vertices in SAA

The curvature of the lipid-binding face in the SAA monomer is defined by the angle between h1 and h3. In the maximally helical state, this angle is critically hinged upon the GPGG motif in the h2-h3 linker (Figs. 2 and 5). This motif, together with several conserved alanines and glycines located nearby, facilitates a tight packing of h1 against h3 at an angle of ~43°, with unusually short main chain spacing of 3.6 Å between A10 and G50 seen in the crystal structures [21]. The EX1 data at 5 °C reveal that in free protein in solution, the region around vertex 1 alternates between highly protected and minimally protected conformations (Fig. 5). The population of the latter progressively increases at 15 and at 25 °C upon helical unfolding in free SAA (Figure S7). This suggests that in SAA in solution, the GPGG linker and its adjacent helices are either unordered as expected of this Gly-rich motif, or are very well-ordered as seen in the crystal structures (Figs. 1D and 2).

In SAA-POPC, the vertex 1 region shifts toward a highly protected conformation (Fig. 5, S7). This suggests that lipid binding selectively stabilizes the pre-existing well-ordered structure in this region, reducing the entropic penalty for lipid binding by this intrinsically disordered protein. Our findings, taken together, are consistent with a mixed model for lipid binding by SAA. The central and C-terminal part of h3 undergoes coupled folding and binding, in line with a mechanism of "induced fit." Lipid-induced structural changes in the central part of h1 and the h2-h3 region at vertex 1 are consistent with a "conformational selection" model, wherein the well-ordered conformation has a low population in the ligand-free state but is selectively stabilized in the ligand-bound state.

Helices h4 and h' mimic the orientation of helices h2 and h3 in the crystal structure (Fig. 2). Like the GPGG motif that forms the h2-h3 turn in vertex 1, the Gly-containing h4-h' turn in vertex 2 positions h4 against h' at an angle of ~45° (Figs. 2A and 5). Like the h2-h3 linker at V_1, the h4-h' linker at V_2 is relatively well ordered in the crystal structures (Fig. 1D) and shows relatively high structural protection in free SAA in solution and in SAA-POPC (Fig. 4). Moreover, like V_1, V_2 shows unusually close interhelical main chain spacing in the crystal structure, including a 3.3 Å distance between C_α of Y42 from h2 and carbonyl O of G86 from h4. Notably, Y42 and G86 are 100% evolutionally conserved, while other residues from the h4-h' linker at V_2 are also highly conserved (Fig. 1). Similarly, the GPGG linker and other residues facilitating unusually tight helical packing in V_1 are 100% conserved [21]. Together, these findings suggest that V_1 and V_2 play similar structural roles in the N- and C-terminal regions of SAA, conferring its unique molecular fold. We speculate that, similar to the V_1 region whose ordered structure is stabilized upon lipid binding via h1 and h3, the ordered structure at V_2 may be stabilized upon ligand binding via the C-terminal part of SAA. Future studies of other SAA ligands will test these hypotheses.

A β-hairpin in SAA monomer may initiate the amyloid formation

Our MD simulations have predicted an unexpected β-hairpin in mSAA1 monomer in solution (Fig. 7B, S10-S12). The HDX MS results at 5–25 °C suggest strongly that the population of this β-hairpin decreases when SAA is in complex with lipid (orange in Fig. 4C, S4C, S5C). In other amyloidogenic proteins, such as Aβ peptide or α-synuclein, early misfolding intermediates are thought to involve activated protein monomers [42,43] that can contain transient β-sheet structure, such as solvent-exposed β-hairpins [44,45]. These aggregation-prone conformations can be stabilized upon protein oligomerization and are ultimately converted into intermolecular cross-β-sheet in amyloid. Therefore, sequestering β-hairpin intermediates has been proposed as a strategy to block amyloid formation by various proteins [44,45].

Our MD simulations suggest the transient formation of a β-hairpin in residues 28–36, with two short β-strands separated by a tight turn at G32, D33

(Fig. 7B, S10-S12). In the crystal structure, which lacks β-sheets, residues 28−36 encompass an interhelical linker h1-h2 and the beginning of h2 at apex 1. Several lines of experimental evidence provide support for β-hairpin formation. First, the lipid-induced decrease (rather than increase) in protection from HDX, which was consistently observed only in this region of SAA (pink in Figs. 4C, S4C, S5C), suggests that, unlike the helical structure that is stabilized upon lipid binding, the ordered structure at apex 1 is destabilized. Second, the h1-h2 region is part of the fibril-forming N-terminal segment found in AA deposits *in vivo*. Third, the two β-strands connected by a tight turn identified in our MD simulations overlap β-strands β4 and β5 (residues 27−29 and 33−38) observed in the amyloid fibril structure formed by a fragment of mSAA1.1 [34] (Fig. 1B).

Together, these findings suggest that local helical unfolding around the h1-h2 linker, which is more likely to occur in free SAA than in SAA-POPC, may lead to a transient β-hairpin formation in this region. This is consistent with the previous finding that at pH~7, SAA binding to HDL [16] or formation of SAA-POPC complexes protects the protein from forming amyloid [18,23]. Although the aromatic cluster involving W29, Y35, and F36 probably contributes to the transient stability of the β-hairpin in mSAA1 (Figure S12), the hairpin residues, GWKDGDKYF, have a high charge content. Therefore, this residue segment is not assigned high amyloidogenic propensity by sequence-based bioinformatics tools, such as AmylPred2 or PASTA2, which are used to predict amyloidogenic segments in soluble proteins (Fig. 1, top) [15]. However, if the formation of this hairpin in monomeric SAA is confirmed, it may represent an aggregation-prone N* state and amyloidogenic intermediate [42,43], and initiate amyloid formation [44,45]. If so, our study reveals a limitation in the existing sequence-based amyloid prediction tools. Since h1-h2 linker regions in hSAA1 and mSAA1 differ in their primary sequence (Fig. 1) and fibril structure [34], the role of this region in β-structure formation in human vis-à-vis murine protein remains to be determined.

Materials and Methods

Protein, lipid, and lipoproteins

Recombinant full-length murine SAA isoform 1.1 (11.6 kDa, 103 amino acids) was used in all experiments. This isoform is termed mSAA2 in the nomenclature based on the gene sequence [46]. SAA was expressed in *E. coli* and purified under denaturing conditions to 95% purity, as described previously [47]. Protein purity and integrity were assessed by SDS PAGE and by mass spectrometry. Lipid 1-palmitoyl-2-oleoyl-*sn*-glycero-3-phosphocholine (POPC; C16:0, C18:1) was 97%+ pure from Avanti Polar Lipids. All other chemicals were of the highest purity analytical grade.

Lyophilized mSAA1, which was stored at 4 °C, was dissolved in double-distilled H_2O; the stock solution was diluted into 10 mM sodium phosphate at pH 7.5 (standard buffer) prior to use. Protein concentrations were determined by UV absorbance at 280 nm using Varian Cary-300 UV−vis spectrophotometer.

Lipoprotein reconstitution and characterization

SAA-containing lipoproteins of controlled size were reconstituted by a cholate dialysis method, as previously described [29]. Briefly, POPC film was dispersed in a standard buffer and solubilized by adding 1 M sodium deoxycholate. The cholate-solubilized POPC was incubated with SAA at 37 °C for 1 h; SAA to POPC molar ratios in the incubation mixture ranged from 1:10 (to obtain lipoproteins ~10 nm in size) to 1:80 (to obtain lipoproteins ~20 nm in size). The lipoprotein solution was dialyzed extensively against the standard buffer. Lipoprotein size and homogeneity were characterized by nondenaturing PAGE and size-exclusion chromatography, and protein and lipoprotein structure and stability were characterized by CD spectroscopy as previously described [29]. The results for SAA and SAA-POPC used in the current study are shown in Figures S1 and S2.

Hydrogen-deuterium exchange mass spectrometry

HDX MS data for free SAA and SAA-POPC were obtained under conditions similar to those previously described [48]. To initiate deuterium labeling of free SAA, 1 μl of 0.5 mg/ml protein in standard buffer (10 mM sodium phosphate, pH 7.5) was diluted 18-fold with labeling buffer (10 mM sodium phosphate, pD 7.5, 99.9% D_2O) at 5, 15 or 25 °C. The labeling was quenched by a 2-fold dilution with ice-cold quench buffer (150 mM sodium phosphate, pH 2.3, H_2O), at time points ranging from 5 s to 4 h. A similar labeling protocol was followed for SAA-POPC. Other HDX experimental parameters, as agreed upon in Ref. [49], are provided in Supplemental Table S1.

Deuterated and control samples were digested with pepsin (10 mg/mL, Sigma P6887; Lot#SLBL1721V) for 5 min on ice, and then injected into an M-class Acquity UPLC with HDX technology (Waters). The cooling chamber of the UPLC system, which housed all the chromatographic elements, was held at 0.0 ± 0.1 °C for the entire time of the measurements. Peptides were trapped and desalted on a VanGuard Pre-Column trap [2.1 mm × 5 mm, ACQUITY UPLC BEH C18, 1.7 μm (Waters, 186002346)] for 3 min at 100 μL/min, eluted from the trap using a 5%−35% gradient of acetonitrile over 6 min at a flow rate of 100 μL/min, and separated using an ACQUITY UPLC HSS T3, 1.8 μm, 1.0 mm × 50 mm column. The back pressure averaged ~12,950 psi at 0 °C and 5% acetonitrile: 95% water. The error of determining the deuterium levels was ±0.30 Da in this experimental setup. The trap column and analytical column were washed with a blank run before each sample. Mass spectra were acquired using a Waters Synapt G2-Si $HDMS^E$ mass spectrometer. The mass spectrometer was calibrated with a direct infusion of a solution of glu-

fibrinopeptide (Sigma, F3261) at 200 fmol/μL at a flow rate of 5 μL/min prior to data collection. A conventional electrospray source was used, and the instrument was scanned 0.4 scans/second over the range 50−2000 m/z with ion mobility engaged. The instrument configuration was the following: capillary was 3.2 kV, trap collision energy at 4 V, sampling cone at 40 V, source temperature of 80 °C, and desolvation temperature of 175 °C. All comparison experiments were done under identical experimental conditions such that deuterium levels were not corrected for back-exchange, and are, therefore, reported as relative. Analyses of SAA alone versus SAA-POPC 1:10 (particles prepared using 1:10 SAA:POPC molar ratio) at 5 °C were performed 4 times, 2 technical replicates each of two different protein batches. Analyses comparing SAA with SAA-POPC 1:10 at 15 °C and 25 °C were performed once at 15 °C and once at 25 °C. Analyses of SAA-POPC lipoproteins obtained using 1:30 or 1:80 SAA:POPC molar ratios were each recorded once at 5 °C for comparison with those obtained using 1:10 M ratio (Figure S6).

Peptides were identified using PLGS 3.0.1 (Waters, RRID: SCR_016664, 720001408EN) using multiple replicates of undeuterated control samples. Raw MS data were imported into DynamX 3.0 (Waters, 720005145EN) and filtered as follows: minimum consecutive products of 2; the minimum number of products per amino acid of 0.2, 10 ppm error. Those peptides meeting the filtering criteria were further processed automatically by DynamX, followed by manual inspection of all processing. The relative amount of deuterium in each peptide was determined by subtracting the centroid mass of the undeuterated form of each peptide from the deuterated form, at each time point, for each condition. The error bars in all the deuterium uptake plots represent variation supplied by DynamX software, which is determined for each peptide using different charge states for all technical and biological replicates. Deuterium uptake values were used to generate uptake graphs and difference maps. All HDX MS data have been deposited to the ProteomeXchange Consortium via the PRIDE [50] partner repository with the dataset identifier PXD016391.

Calculations to adjust for changes to the intrinsic rates of exchange at different temperatures were performed as described in Ref. [35]. The measured relative percent deuteration at each timepoint for each peptide at 5 °C was adjusted mathematically to what it would be at 15 °C or 25 °C by multiplying by the correction factors of 2.4087 or 5.4696 (respectively). These calculations and the results are found in Supplemental Dataset 1. Alternatively, the measured exchange at 15 °C and 25 °C was adjusted mathematically to what it would be at 5 °C by dividing by the correction factors of 2.4087 or 5.4696 (respectively), also shown in Supplemental Dataset 1. The correction factors for the temperature differences in this study were determined using the Arrhenius equation found in Ref. [35].

Molecular dynamics simulations

SAA monomer alone or with a POPC micelle was simulated as outlined in Figure S8. All simulations were performed using the GROMACS 2018.3 package [51], employing the CHARMM36m force field for proteins [52] and CHARMM36 force field for lipids [53]. Structures were rendered using VMD [54]. The analyses were conducted with in-house Python scripts utilizing NumPy, SciPy, and MDAnalysis libraries [55]. Protein secondary structure was assigned using the STRIDE algorithm in VMD [56]. All-atom protein simulations were conducted in an aqueous environment, defined by the TIP3P water model [57], with 150 mM NaCl. The temperature was maintained with the Nosé-Hoover thermostat [58,59] and the pressure was held at 1 atm and Parrinello-Rahman barostat [60]. The initial system configurations were constructed and equilibrated according to the CHARMM-GUI protocols [61]. The 2.2 Å resolution x-ray crystal structure of full-length human SAA1 (PDB ID: 4IP8) was equilibrated at 310 K for 2 μs, and point substitutions at positions differing between hSAA1 and mSAA1 (shown in Figure S9) were introduced to obtain a model of mSAA1.

For analyzing free SAA in solution, this model was simulated at 370 K for 3.8 μs to encourage helical unfolding, from 68% α-helix in the starting configuration (SAA_{68}) to under 30% detected by CD spectroscopy in solution at 5 °C. The protein structures from the final microsecond of the trajectory, where the average helicity was 30%, were clustered employing GROMOS clustering algorithms [62] to extract three solution structures corresponding to the most populated clusters, collectively termed SAA_{30}. Each of these three representative structures was simulated for 500 ns, and the results (termed SAA_{R1} - SAA_{R3}) were used for analysis.

In SAA-POPC simulations, the micelle containing 72 POPC molecules was constructed using Packmol [63] and equilibrated in an aqueous environment for 200 ns, whereupon the protein was placed alongside. In one series of studies, each of the three representative SAA_{30} structures was simulated with the micelle at 310 K for 1 μs. The resulting structures, termed SAA-$POPC_{R1}$ to SAA-$POPC_{R3}$, were used to access the lipid effects on the protein secondary structure (Figure S10; Fig. 7B). In other studies, SAA_{68} was simulated with the POPC micelle at 310 K for 1 μs, and the resulting model, termed SAA-$POPC_{68}$, was used to assess protein-lipid contacts (Fig. 8). The last 500 ns of each simulation were used for analysis.

Funding

This study was supported by the National Institutes of Health grants GM067260, GM135158 (OG), T32 HL007969 (NF), and GM107703 (JES), a research collaboration with the Waters Corporation (JRE), the National Science Foundation CHE-1900416 (JES), the Stewart Amyloidosis Endowment Fund and Weston Visiting Professorship program at the Weizmann Institute of Science, Israel (OG), and the Deutsche Forschungsgemeinschaft grant FA456/15−1 (MF).

Acknowledgements

The authors are indebted to Dr. Shobini Jayaraman for generating Fig. S1, for invaluable help with the lipoprotein characterization, and for many useful discussions.

Author contributions

Nicholas M. Frame (conceptualization, data acquisition and analysis, graphics preparation, writing original draft). Meera Kumanan (data acquisition and analysis, graphics preparation and editing, text writing). Thomas E. Wales (conceptualization, data acquisition and analysis, data submission to the data base, graphics preparation, text editing). Asanga Bandara (conceptualization, data acquisition and analysis, graphics preparation, text writing). Marcus Fändrich (providing critical resources, manuscript editing, funding). John E. Straub (conceptualization, supervision, critical resources, writing and editing, funding). John R. Engen (conceptualization, project administration, supervision, critical resources, writing and editing, data preparation and submission, funding). Olga Gursky (conceptualization, project administration, supervision, writing and editing text and graphics, funding).

Conflicts of interest

The authors declare no conflicts of interest. The content is solely the responsibility of the authors and does not necessarily represent the official views of the National Institutes of Health or any other funding agencies.

Appendix A. Supplementary data

Supplementary data to this article can be found online at https://doi.org/10.1016/j.jmb.2020.01.029.

Received 26 November 2019;
Received in revised form 21 January 2020;
Accepted 21 January 2020
Available online 06 February 2020

Keywords:
hydrogen-deuterium exchange mass spectrometry;
molecular dynamics simulations;
lipoprotein nanoparticle;
β-hairpin misfolding intermediate;
inflammation and immunity

Abbreviations used:
SAA, serum amyloid A; AA, amyloid A; mSAA1, murine SAA isoform 1; hSAA1, human SAA isoform 1; HDL, high-density lipoprotein; POPC, 1-palmitoyl-2-oleoyl-sn-glycero-3-phosphocholine; CD, circular dichroism; HDX, hydrogen-deuterium exchange; MS, mass spectrometry; MD, molecular dynamics.

References

[1] S. Urieli-Shoval, R.P. Linke, Y. Matzner, Expression and function of serum amyloid A, a major acute-phase protein, in normal and disease states, Curr. Opin. Hematol. 7 (2000) 64–69.
[2] K.K. Eklund, K. Niemi, P.T. Kovanen, Immune functions of serum amyloid A, Crit. Rev. Immunol. 32 (4) (2012) 335–348.
[3] G.T. Westermark, M. Fändrich, P. Westermark, AA amyloidosis: pathogenesis and targeted therapy, Annu. Rev. Pathol. 10 (2015) 321–344.
[4] R. Papa, H.J. Lachmann, Secondary, AA, amyloidosis, Rheum. Dis. Clin. N. Am. 44 (4) (2018) 585–603.
[5] P. Shridas, L.R. Tannock, Role of serum amyloid A in atherosclerosis, Curr. Opin. Lipidol. 30 (4) (2019) 320–325.
[6] C.M. Uhlar, C.J. Burgess, P.M. Sharp, A.S. Whitehead, Evolution of the serum amyloid A (SAA) protein superfamily, Genomics 19 (2) (1994) 228–235.
[7] L. Sun, R.D. Ye, Serum amyloid A1: structure, function and gene polymorphism, Gene 583 (1) (2016) 48–57.
[8] M. De Buck, M. Gouwy, J.M. Wang, J. Van Snick, G. Opdenakker, S. Struyf, J. Van Damme, Structure and expression of different serum amyloid A (SAA) variants and their concentration-dependent functions during host insults, Curr. Med. Chem. 23 (2016) 1725–1755.
[9] R.D. Ye, L. Sun, Emerging functions of serum amyloid A in inflammation, J. Leukoc. Biol. 98 (6) (2015) 923–929.
[10] C.M. Uhlar, A.S. Whitehead, Serum amyloid A, the major vertebrate acute-phase reactant, Eur. J. Biochem. 265 (1999) 501–523.
[11] G.H. Sack Jr., Serum amyloid A - a review, Mol. Med. 24 (1) (2018) 46.
[12] E.P. Benditt, N. Eriksen, Amyloid protein SAA is associated with high density lipoprotein from human serum, Proc. Natl. Acad. Sci. U.S.A. 74 (1977) 4025–4028.
[13] R. Kisilevsky, P.N. Manley, Acute-phase serum amyloid A: perspectives on its physiological and pathological roles, Amyloid 19 (2012) 5–14.
[14] P.G. Wilson, J.C. Thompson, P. Shridas, P.J. McNamara, M.C. de Beer, F.C. de Beer, N.R. Webb, L.R. Tannock, Serum amyloid A is an exchangeable apolipoprotein, Arterioscler. Thromb. Vasc. Biol. 38 (8) (2018) 1890–1900.
[15] M. Das, O. Gursky, Amyloid-forming properties of human apolipoproteins: sequence analyses and structural insights, Adv. Exp. Med. Biol. 855 (2015) 175–211.
[16] S. Claus, K. Meinhardt, T. Aumüller, I. Puscalau-Girtu, J. Linder, C. Haupt, P. Walther, T. Syrovets, T. Simmet, M. Fändrich, Cellular mechanism of fibril formation from

serum amyloid A1 protein, EMBO Rep. 18 (8) (2017) 1352–1366.
[17] S. Jayaraman, D.L. Gantz, C. Haupt, M. Fändrich, O. Gursky, Serum amyloid A sequesters diverse phospholipids and their hydrolytic products, hampering fibril formation and proteolysis in a lipid-dependent manner, Chem. Commun. 54 (28) (2018) 3532–3535.
[18] J.S. Liang, B.M. Schreiber, M. Salmona, G. Phillip, W.A. Gonnerman, F.C. de Beer, J.D. Sipe, Amino terminal region of acute phase, but not constitutive, serum amyloid A (apoSAA) specifically binds and transports cholesterol into aortic smooth muscle and HepG2 cells, J. Lipid Res. 37 (10) (1996) 2109–2116.
[19] H. Takase, H. Furuchi, M. Tanaka, T. Yamada, K. Matoba, K. Iwasaki, T. Kawakami, T. Mukai, Characterization of reconstituted high-density lipoprotein particles formed by lipid interactions with human serum amyloid A, Biochim. Biophys. Acta 1842 (10) (2014) 1467–1474.
[20] S. Jayaraman, C. Haupt, O. Gursky, Thermal transitions in serum amyloid A in solution and on the lipid: implications for structure and stability of acute-phase HDL, J. Lipid Res. 56 (8) (2015) 1531–1542.
[21] N.M. Frame, O. Gursky, Structure of serum amyloid A suggests a mechanism for selective lipoprotein binding and functions: SAA as a hub in macromolecular interaction networks, FEBS Lett. 590 (6) (2016) 866–879.
[22] M. Tanaka, A. Nishimura, H. Takeshita, H. Takase, T. Yamada, T. Mukai, Effect of lipid environment on amyloid fibril formation of human serum amyloid A, Chem. Phys. Lipids 202 (2017) 6–12.
[23] S. Jayaraman, D.L. Gantz, C. Haupt, O. Gursky, Serum amyloid A forms stable oligomers that disrupt vesicles at lysosomal pH and contribute to the pathogenesis of reactive amyloidosis, Proc. Natl. Acad. Sci. U.S.A. 114 (32) (2017) E6507–E6515.
[24] S. Jayaraman, C. Haupt, O. Gursky, Paradoxical effects of SAA on lipoprotein oxidation suggest a new antioxidant function for SAA, J. Lipid Res. 57 (12) (2016) 2138–2149.
[25] M.G. Derebe, C.M. Zlatkov, S. Gattu, K.A. Ruhn, S. Vaishnava, G.E. Diehl, J.B. MacMillan, N.S. Williams, L.V. Hooper, Serum amyloid A is a retinol binding protein that transports retinol during bacterial infection, eLife 3 (2014), e03206.
[26] Z. Hu, Y.J. Bang, K.A. Ruhn, L.V. Hooper, Molecular basis for retinol binding by serum amyloid A during infection, Proc. Natl. Acad. Sci. U.S.A. 116 (38) (2019) 19077–19082.
[27] S. Jayaraman, M. Fändrich, O. Gursky, Synergy between serum amyloid A and secretory phospholipase A2 suggests a vital role for an ancient protein in lipid clearance, eLife 46630 (1) (2019) 200–210.
[28] J.A. Stonik, A.T. Remaley, S.J. Demosky, E.B. Neufeld, A. Bocharov, H.B. Brewer, Serum amyloid A promotes ABCA1-dependent and ABCA1-independent lipid efflux from cells, Biochem. Biophys. Res. Commun. 321 (4) (2004) 936–941.
[29] N.M. Frame, S. Jayaraman, D.L. Gantz, O. Gursky, Serum amyloid A self-assembles with phospholipids to form stable protein-rich nanoparticles with a distinct structure: a hypothetical function of SAA as a "molecular mop" in immune response, J. Struct. Biol. 200 (3) (2017) 293–302.
[30] W. Colón, J.J. Aguilera, S. Srinivasan, Intrinsic stability, oligomerization, and amyloidogenicity of HDL-free serum amyloid A, Adv. Exp. Med. Biol. 855 (2015) 117–134.
[31] J. Lu, Y. Yu, I. Zhu, Y. Cheng, P.D. Sun, Structural mechanism of serum amyloid A-mediated inflammatory amyloidosis, Proc. Natl. Acad. Sci. U.S.A. 111 (14) (2014) 5189–5194.
[32] H. Patel, J. Bramall, H. Waters, M.C. De Beer, P. Woo, Expression of recombinant human serum amyloid A in mammalian cells and demonstration of the region necessary for high-density lipoprotein binding and amyloid fibril formation by site-directed mutagenesis, Biochem. J. 318 (3) (1996) 1041–1049.
[33] L. Wang, W. Colón, The interaction between apolipoprotein serum amyloid A and high-density lipoprotein, Biochem. Biophys. Res. Commun. 317 (1) (2004) 157–361.
[34] F. Liberta, S. Loerch, M. Rennegarbe, A. Schierhorn, P. Westermark, G.T. Westermark, B.P.C. Hazenberg, N. Grigorieff, M. Fändrich, M. Schmidt, Cryo-EM fibril structures from systemic AA amyloidosis reveal the species complementarity of pathological amyloids, Nat. Commun. 10 (1) (2019) 1104.
[35] J.R. Engen, T.E. Wales, X. Shi, Hydrogen exchange mass spectrometry for conformational analysis of proteins, in: Encyclopedia of Analytical Chemistry, John Wiley, Chichester. R. A. Meyers, 2011, https://doi.org/10.1002/9780470027318.a9201.
[36] S. Patke, S. Srinivasan, R. Maheshwari, S.K. Srivastava, J. J Aguilera, W. Colón, R.S. Kane, Characterization of the oligomerization and aggregation of human Serum Amyloid A, PloS One 8 (6) (2013) e64974.
[37] D.M. Ferraro, N. Lazo, A.D. Robertson, EX1 hydrogen exchange and protein folding, Biochemistry 43 (3) (2004) 587–594.
[38] D.D. Weis, T.E. Wales, J.R. Engen, M. Hotchko, L.F. Ten Eyck, Identification and characterization of EX1 kinetics in H/D exchange mass spectrometry by peak width analysis, J. Am. Soc. Mass Spectrom. 17 (11) (2006) 1498–1509.
[39] F.J. Stevens, Hypothetical structure of human serum amyloid A protein, Amyloid 11 (2004) 71–80.
[40] D. Neculai, M. Schwake, M. Ravichandran, F. Zunke, R.F. Collins, J. Peters, M. Neculai, J. Plumb, P. Loppnau, J.C. Pizarro, A. Seitova, W.S. Trimble, P. Saftig, S. Grinstein, S. Dhe-Paganon, Structure of LIMP-2 provides functional insights with implications for SR-BI and CD36, Nature 504 (7478) (2013) 172–176.
[41] K.S. Conrad, T.W. Cheng, D. Ysselstein, S. Heybrock, L.R. Hoth, B.A. Chrunyk, C.W. Am Ende, D. Krainc, M. Schwake, P. Saftig, S. Liu, X. Qiu, M.D. Ehlers, Lysosomal integral membrane protein-2 as a phospholipid receptor revealed by biophysical and cellular studies, Nat. Commun. 8 (1) (2017) 1908.
[42] J.E. Straub, D. Thirumalai, Principles governing oligomer formation in amyloidogenic peptides, Curr. Opin. Struct. Biol. 20 (2) (2010) 187–195.
[43] J.E. Straub, D. Thirumalai, Toward a molecular theory of early and late events in monomer to amyloid fibril formation, Annu. Rev. Phys. Chem. 62 (2011) 437–463.
[44] W. Hoyer, C. Grönwall, A. Jonsson, S. Ståhl, T. Härd, Stabilization of a β-hairpin in monomeric Alzheimer's amyloid-β peptide inhibits amyloid formation, Proc. Natl. Acad. Sci. U.S.A. 105 (13) (2008) 5099–5104.
[45] A.A. Orr, H. Shaykhalishahi, E.A. Mirecka, S.V.R. Jonnalagadda, W. Hoyer, P. Tamamis, Elucidating the multi-targeted anti-amyloid activity and enhanced islet amyloid polypeptide binding of β-wrapins, Comput. Chem. Eng. 116 (2018) 322–332.

[46] J. Sipe, Revised nomenclature for serum amyloid A (SAA), Nomencl Committ. Int. Soc. Amyloidosis vol. 6 (1) (1999) 67–70. Part 2, Amyloid.
[47] M. Kollmer, K. Meinhardt, C. Haupt, F. Liberta, M. Wulff, J. Linder, L. Handl, L. Heinrich, C. Loos, M. Schmidt, T. Syrovets, T. Simmet, P. Westermark, G.T. Westermark, U. Horn, V. Schmidt, P. Walther, M. Fändrich, Electron tomography reveals the fibril structure and lipid interactions in amyloid deposits, Proc. Natl. Acad. Sci. U.S.A. 113 (20) (2016) 5604–5609.
[48] M. Das, C.J. Wilson, X. Mei, T.E. Wales, J.R. Engen, O. Gursky, Structural stability and local dynamics in disease-causing mutants of human apolipoprotein A-I: what makes the protein amyloidogenic? J. Mol. Biol. 428 (2 Pt B) (2016) 449–462.
[49] G.R. Masson, J.E. Burke, N.G. Ahn, G.S. Anand, C. Borchers, S. Brier, G.M. Bou-Assaf, J.R. Engen, S.W. Englander, J. Faber, R. Garlish, P.R. Griffin, M.L. Gross, M. Guttman, Y. Hamuro, A.J.R. Heck, D. Houde, R.E. Iacob, T.J.D. Jørgensen, I.A. Kaltashov, J.P. Klinman, L. Konermann, P. Man, L. Mayne, B.D. Pascal, D. Reichmann, M. Skehel, J. Snijder, T.S. Strutzenberg, E.S. Underbakke, C. Wagner, T.E. Wales, B.T. Walters, D.D. Weis, D.J. Wilson, P.L. Wintrode, Z. Zhang, J. Zheng, D.C. Schriemer, K.D. Rand, Recommendations for performing, interpreting and reporting hydrogen deuterium exchange mass spectrometry (HDX-MS) experiments, Nat. Methods 16 (7) (2019) 595–602.
[50] Y. Perez-Riverol, A. Csordas, J. Bai, M. Bernal-Llinares, S. Hewapathirana, D.J. Kundu, A. Inuganti, J. Griss, r. G. Maye, M. Eisenacher, E. Pérez, J. Uszkoreit, J. Pfeuffer, T. Sachsenberg, z. S. Yilma, S. Tiwary, J. Cox, E. Audain, M. Walzer, A.F. Jarnuczak, T. Ternent, A. Brazma, J.A. Vizcaíno, The PRIDE database and related tools and resources in 2019: improving support for quantification data, Nucleic Acids Res. 47 (D1) (2019) D442–D450.
[51] M.J. Abraham, T. Murtola, R. Schulz, S. Páll, J.C. Smith, B. Hess, E. Linda h, Gromacs: high performance molecular simulations through multi-level parallelism from laptops to supercomputers, SoftwareX 1–2 (2015) 19–25.
[52] J. Huang, S. Rauscher, G. Nawrocki, T. Ran, M. Feig, B.L. de Groot, H. Grubmüller, A.D. MacKerell, CHARMM36m: an improved force field for folded and intrinsically disordered proteins, Nat. Methods 14 (1) (2017) 71–73.
[53] J.B. Klauda, R.M. Venable, J.A. Freites, J.W. O'Connor, D.J. Tobias, C. Mondragon-Ramirez, I. Vorobyov, A.D. MacKerell Jr., R.W. Pastor, Update of the CHARMM all-atom additive force Field for lipids: validation on six lipid types, J. Phys. Chem. B 114 (23) (2010) 7830–7843.
[54] W. Humphrey, A. Dalke, K. Schulten, VMD: visual molecular dynamics, J. Mol. Graph. 14 (1) (1996) 33–38.
[55] R. Gowers, M. Linke, J. Barnoud, T. Reddy, M. Melo, r. S. Seyle, J. Domanski, D.L. Dotson, S. Buchouxk, I.M. Kenney, O. Beckstein, MDAnalysis: a Python package for the rapid analysis of molecular dynamics simulations, Proceedings of the 15th Python in Science Conference (Scipy), 2018, pp. 98–105.
[56] M. Heinig, D. Frishman, STRIDE: a web server for secondary structure assignment from known atomic coordinates of proteins, Nucleic Acids Res. 32 (2004) W500–W502.
[57] W.L. Jorgensen, J. Chandrasekhar, J.D. Madura, R.W. Impey, M.L. Klein, Comparison of simple potential functions for simulating liquid water, J. Chem. Phys. 79 (2) (1983) 926–935.
[58] W.G. Hoover, Canonical dynamics: equilibrium phase-space distributions, Phys. Rev. A 31 (3) (1985) 1695–1697.
[59] S. Nosé, A unified formulation of the constant temperature molecular dynamics methods, J. Chem. Phys. 81 (1) (1984) 511–519.
[60] M. Parrinello, A. Rahman, Polymorphic transitions in single crystals: a new molecular dynamics method, J. Appl. Phys. 52 (12) (1981) 7182–7190.
[61] S. Jo, X. Cheng, J. Lee, S. Kim, S.-J. Park, D.S. Patel, A.H. Beaven, K.I. Lee, H. Rui, S. Park, H.S. Lee, B. Roux, A.D. MacKerell Jr., J.B. Klauda, Y. Qi, W. Im, CHARMM-GUI 10 years for biomolecular modeling and simulation, J. Comput. Chem. 38 (15) (2017) 1114–1124.
[62] X. Daura, K. Gademann, B. Jaun, h. D. Seebac, W.F. van Gunsteren, A.E. Mark, Peptide folding: when simulation meets experiment, Angew. Chem. Int. 38 (1–2) (1999) 236–240.
[63] L. Martínez, R. Andrade, E.G. Birgin, J.M. Martínez, PACKMOL: a package for building initial configurations for molecular dynamics simulations, J. Comput. Chem. 30 (13) (2009) 2157–2164.
[64] F. Sievers, A. Wilm, D. Dineen, T.J. Gibson, K. Karplus, W. Li, R. Lopez, H. McWilliam, M. Remmert, J. Söding, J. D Thompson, D.G. Higgins, Fast, scalable generation of high-quality protein multiple sequence alignments using Clustal Omega, Mol. Syst. Biol. 7 (2011) 539.
[65] A.M. Waterhouse, J.B. Procter, D.M.A. Martin, M. Clamp, n. G.J. Barto, Jalview Version 2 - a multiple sequence alignment editor and analysis workbench, Bioinformatics 25 (9) (2009) 1189–1191. http://www.jalview.org/.
[66] A. Waterhouse, M. Bertoni, S. Bienert, G. Studer, G. Tauriello, G.R. umienny, F.T. Heer, T.A.P. de Beer, C. Rempfer, L. Bordoli, R. Lepore, T. Schwede, SWISS-MODEL: homology modelling of protein structures and complexes, Nucleic Acids Res. 46 (W1) (2018) W296–W303.